Dopant site selectivity in $BaCe_{0.85}M_{0.15}O_{3-\delta}$ by extended x-ray absorption fine structure

J. Wu
Material Science, California Institute of Technology, Pasadena, California 91125

S. M. Webb and S. Brennan
Stanford Synchrotron Radiation Laboratory, Stanford, California 94309

S. M. Haile
Material Science, California Institute of Technology, Pasadena, California 91125

(Received 17 February 2004; accepted 12 November 2004; published online 10 February 2005)

Rare earth doped $BaCeO_3$ has been widely investigated as a proton conducting material. Trivalent dopants are generally assumed to fully occupy the Ce^{4+}-site, and thereby introduce oxygen vacancies into the perovskite structure. Recent studies indicate the possibility of partial dopant incorporation onto the Ba^{2+}-site concomitant with BaO evaporation, reducing the oxygen vacancy content. Because proton incorporation requires, as a first step, the generation of oxygen vacancies such dopant partitioning is detrimental to protonic conductivity. A quantitative Extended X-ray Absorption Fine Structure (EXAFS) study of $BaCe_{0.85}M_{0.15}O_{3-\delta}$(M=Yb,Gd) is presented here along with complementary x-ray powder diffraction and electron probe chemical analyses. The EXAFS results demonstrate that as much as 4.6% of the ytterbium and 7.2% of the gadolinium intended for incorporation onto the Ce site, in fact, resides on the Ba site. The results are in qualitative agreement with the diffraction and chemical analyses, which additionally show an even greater extent of Nd incorporation on the Ba site. © *2005 American Institute of Physics*. [DOI: 10.1063/1.1846946]

I. INTRODUCTION

The high proton conductivity of rare-earth (or yttrium) doped $BaCeO_3$ has generated interest in its applicability in reduced temperature solid oxide fuel cells and in hydrogen sensors.[1–3] Proton incorporation requires, as a first step, the generation of oxygen vacancies via trivalent ion doping on the tetravalent ion site. In a subsequent step, exposure of the doped material to humid atmospheres results in the incorporation of hydroxyl groups on formerly vacant oxygen sites and protons at other oxygen sites. The two steps are illustrated by Eqs. (1) and (2):

$$2Ce_{Ce}^{x} + O_{o}^{x} + M_2O_3 \rightarrow 2M'_{Ce} + V_{o}^{\bullet} + 2CeO_2 \quad (1)$$

$$H_2O(g) + V_{o}^{\bullet} + O_{o}^{x} \rightarrow 2OH_{o}^{\bullet} \quad (2)$$

If all oxygen vacancies are filled during the humidification step, the proton concentration is simply equal to the dopant concentration, $[OH_o^{\bullet}]=[M'_{Ce}]$. Alternative hydration pathways in which electron holes are the charge compensating defects for dopant ions and which are later exchanged with protons under hydrogen atmospheres lead to an identical result for the maximum proton content.

In a series of earlier studies,[4–7] extensive evidence was presented that Eq. (1) does not, in fact, adequately describe the trivalent incorporation mechanism in barium cerate. Particularly in the case of large dopant cations, dopant partitioning can occur such that a non-negligible concentration of trivalent species resides on the Ba site. This is accompanied by some barium oxide evaporation at high temperatures, ensuring that the overall A:B mole ratio in the ABO_3 perovskite remains close to 1:1. Such an incorporation onto the ('wrong') site was used to explain the observation that water uptake and proton conductivity increased in doped barium cerate in the order Nd<Gd<Yb, where Nd has the largest ionic radius in the series and Yb the smallest. This same sequence, in terms of water uptake, was reported earlier by Stevenson *et al.*,[8] but with a little interpretation. Dopant partitioning has also been interpreted to be responsible for the unusual observation that the cell volume of doped barium cerate increased in the sequence Yb<Nd<Gd, in a non-monotonic dependence on a dopant ionic radius.[6] This result can be understood if the concentration of Nd on the Ba site is great enough that cell expansion due to incorporation on the Ce site is mitigated by cell contraction due to incorporation on the Ba site $[R(Ba^{2+})>R(Nd^{3+})>R(Ce^{4+})]$.

While all of the data, obtained from a variety of techniques including x-ray powder diffraction, electron microprobe chemical analysis, thermal gravimetric analysis and ac impedance spectroscopy, are consistent with a model of dopant partitioning and increasing incorporation onto the Ba site with increasing dopant ionic radius, direct experimental observation of the dopant location has not yet been achieved. In this work, we employ extended x-ray absorption fine structure spectroscopy (EXAFS) to directly probe the local environment about the dopant species (Yb and Gd) and establish their site preferences.

II. METHODOLOGY

Extended x-ray absorption spectroscopy measures the x-ray absorption coefficient, μ, as a function of photon en-

TABLE I. Nearest neighbor distances about the Ba atom located at 0.001, 0.023, 0.250 in $BaCeO_3$ and their atomic coordinates, after Knight *et al.* (see Ref. 10).

Atom	Distance (Å)	*x* (frac. coor.)	*y* (frac. coor.)	*z* (frac. coor.)
O1	3.3603	0.071	−0.513	0.250
O1	2.9171	0.071	0.487	0.250
O1	3.5739	−0.571	−0.013	0.250
O1	2.6783	0.429	−0.013	0.250
O2	2.9695	−0.274	0.278	0.041
O2	3.5948	0.274	−0.278	0.541
O2	3.1658	0.226	0.222	−0.041
O2	2.7727	−0.226	−0.222	0.459
O2	3.5948	0.274	−0.278	−0.041
O2	2.9695	−0.274	0.278	0.459
O2	2.7727	−0.226	−0.222	0.041
O2	3.1658	0.226	0.222	0.541
Ce	3.9222	0	−0.500	0
Ce	3.6887	0	0.500	0
Ce	3.9222	0	−0.500	0.500
Ce	3.6887	0.00	0.500	0.500
Ce	3.8204	−0.500	0	0
Ce	3.8102	0.500	0	0
Ce	3.8204	−0.500	0	0.500
Ce	3.8102	0.500	0	0.500

TABLE II. Nearest neighbor distances about the Ce atom located at 0.0, 0.5, 0.0, in $BaCeO_3$ and their atomic coordinates, after Knight *et al.* (see Ref. 10).

Atom	Distance (Å)	x (frac. coor.)	y (frac. coor.)	z (frac. coor.)
O1	2.2399	0.071	0.487	0.250
O1	2.2399	−0.071	0.513	−0.250
O2	2.2256	−0.274	0.278	0.041
O2	2.2587	0.226	0.222−	-0.041
O2	2.2256	0.274	0.722	−0.041
O2	2.2587	−0.226	0.778	0.041
Ba	3.6887	0.001	0.023	0.250
Ba	3.9222	0.001	1.023	0.250
Ba	3.9222	−0.001	−0.023	−0.250
Ba	3.6887	−0.001	0.977	−0.250
Ba	3.8102	−0.499	0.477	−0.250
Ba	3.8204	0.501	0.477	−0.250
Ba	3.8204	−0.501	0.523	0.250
Ba	3.8102	0.499	0.523	0.250

ergy, *E*, above the threshold of an absorption edge. EXAFS spectra typically refer to the range 40–1000 eV beyond the absorption edge. Above the absorption edge, weak oscillations are observed which arise from the constructive and destructive interference between the outgoing photoelectron wave from the core absorbing atom and the backscattered photoelectron wave from the near neighbors of the absorbing atom. The Fourier transformation of the oscillatory spectra yields a radial distribution function in real space which gives information about the local environmental of the absorbing atom.[9]

The two cation sites in ABO_3 perovskites exhibit different coordination numbers, with the A^{2+}-site being 12-fold coordinated and the B^{4+}-site being 6-fold coordinated. Consequently, the EXAFS spectra from dopants on one or the other of these two sites will differ, enabling the establishment of the dopant location in the structure. Indeed, EXAFS has already proved to be a useful tool for locating Yb and Nd in $CaZrO_3$.[10]

In their analysis of $CaZrO_3$, Davies *et al.*[10] assumed single site selectivity, that is, that the dopant was either entirely incorporated onto the A site or entirely onto the B site. In the case of $BaCeO_3$, there is ample evidence that dopants can partition over the two sites and partially occupy both positions, complicating an analysis of the EXAFS data. In the approach here, we model the data for the two extremes of single site selectivity, and proportionately superimpose these two cases to fit the experimental data and describe the physical situation.

Because the structure of undoped $BaCeO_3$ has been well investigated over a wide temperature range, it is straightforward to establish the nearest neighbors to the central absorbing atom, for both the A^{2+} and the B^{4+} sites, as well as the distances to those neighbors. The data are summarized in Tables I and II, using Ba and Ce as the central atom, respectively, and assuming the structure of $BaCeO_3$ reported by Knight *et al.*[11] [orthorhombic with $a=6.23573(3)$, $b=6.21611(4)$, $c=8.77694(5)$Å]. These data serve as the input for the two extremes of single site selectivity.

To address the question of site partition probabilities, we introduce the fitting parameter *frac*. This parameter represents the amount of dopant incorporated onto the B^{4+}-site, by atomic percentage, whereas *1-frac* is used to represent the amount that is incorporated onto the A^{2+}-site. It is evident that the numerical range of *frac* is [0, 1]. Using this formalism, the total EXAFS amplitude is described as[9]

$$\chi(k) = (1 - frac)\sum_i N_i S_l(k) F_i(k) e^{-2\sigma_i^2 k^2} e^{-2r_i/\lambda_i(k)} \times \frac{\sin(2kr_i + \phi_{il}(k))}{kr_i^2} + frac\sum_j N_j S_l(k) F_j(k) e^{-2\sigma_j^2 k^2} \times e^{-2r_j/\lambda_j(k)} \frac{\sin(2kr_j + \phi_{jl}(k))}{kr_j^2}, \quad (3)$$

where N_i is the atom number of the *i*th shell, $S_l(k)$ is the amplitude reduction factor due to many body effects at the

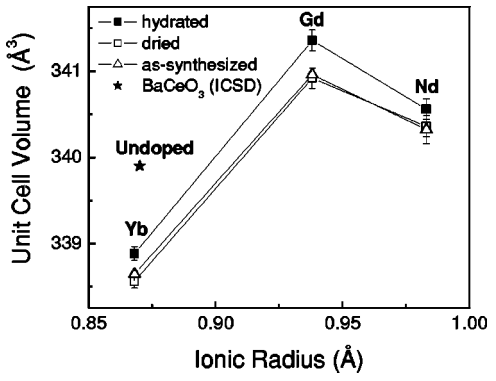

FIG. 1. Cell volume of $BaCe_{0.85}M_{0.15}O_{3-\delta}$ (M=Nd, Gd, Yb, calcined at 1300 °C/10 h, after hydrated, dried, and as-synthesized treatment) as a function of the ionic radius of the dopant species, as determined by x-ray powder diffraction.

TABLE III. Radii of relevant ions.[a]

	$R^{CN(12)}$ Å	$R^{CN(6)}$ Å
Ba^{2+}	1.61	
O^{2-}		1.40
Ce^{4+}		0.87
Nd^{3+}	1.27	0.983
Gd^{3+}		0.938
Yb^{3+}		0.868

[a]Reference 13.

central atom denoted by l which is linked to be the same to every path in our study, F_i is the backscattering amplitude from the ith type of atom, σ_i is the Debye–Waller factor representing the thermal vibration and static disorder, r_i is the distance between the absorber and the ith shell atoms, Φ_{il} is the total phase shift experienced by the photoelectron, λ_i is the electron mean free path and the term $e^{-2ri/\lambda i}$ is due to inelastic losses in the scattering process. Because of the low symmetry of the distorted orthorhombic perovskite structure, there are no more than two atoms (and in some case only one atom) per shell.

The analysis of EXAFS data generally involves background removal, normalization and μ_0 correction, conversion of energy, E, to wave vector, k, the application of a weighting scheme, Fourier transformation of the data and, finally, model refinement to fit the processed data. An analysis in the present study focuses on the deduction of the parameter *frac*, which is accomplished in the final stage of model refinement. In addition, the M(Ba-site)–O, M(Ce-site)–O, M(Ce-site)–Ba, M(Ba-site)–Ce distances, the linked Debye–Waller (thermal displacement) factors and the parameter E_0 (used in the conversion from energy to wave vector) have been fitted as well.

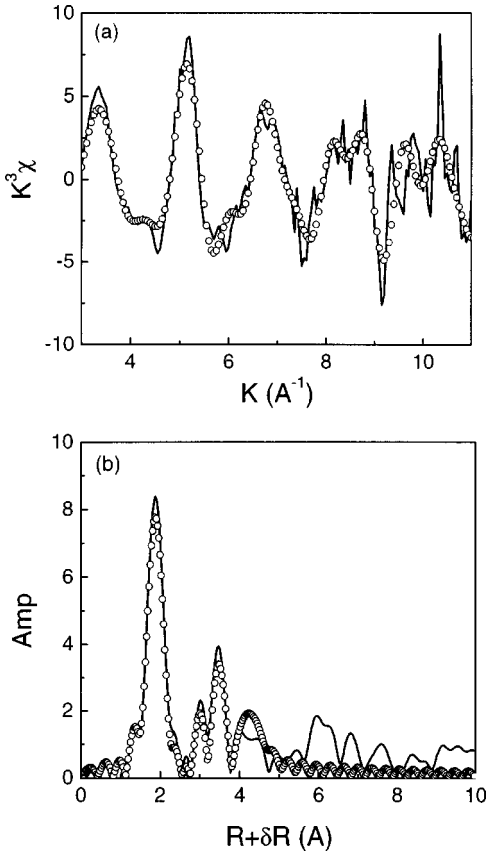

FIG. 2. Gd L_{III} edge EXAFS for $BaCe_{0.85}Gd_{0.15}O_{3-\delta}$ measured at 10 K: experimental data (solid line), best fit data (open circles); (a) the normalized EXAFS spectrum (k^3 weighted); and (b) the Fourier transform without the phase shift.

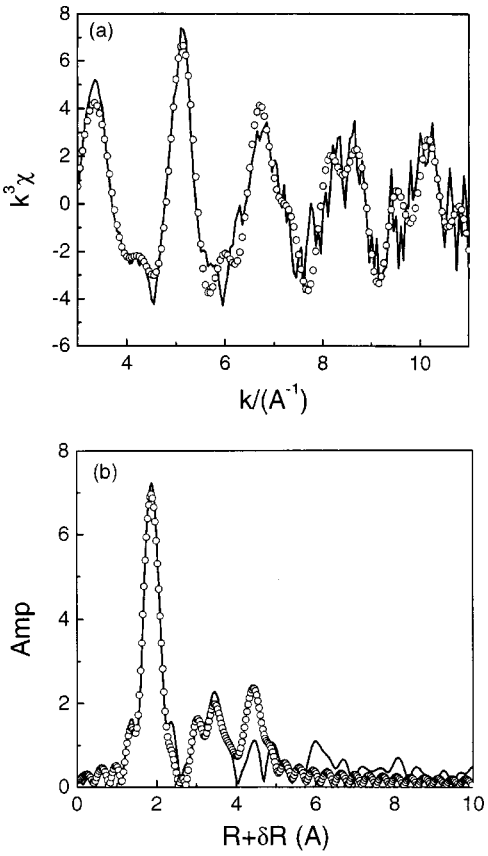

FIG. 3. Gd L_{III} edge EXAFS for $BaCe_{0.85}Gd_{0.15}O_{3-\delta}$ measured at 300 K: experimental data (solid line), best fit data (open circles); (a) the normalized EXAFS spectrum (k^3 weighted), and (b) the Fourier transform without the phase shift.

Extended x-ray absorption measurements on $BaCe_{0.85}Gd_{0.15}O_{3-\delta}$ and $BaCe_{0.85}Yb_{0.15}O_{3-\delta}$ were performed on beam line 2–3 at the Stanford Synchrotron Radiation Laboratory (SSRL) at both liquid helium and room temperatures. Due to the overlap between the Nd L-edges and those of Ba and Ce, no EXAFS data were collected for that dopant. The powders, synthesized as described below, were diluted in BN powder at a 50/50 ratio. A Si (111) double crystal monochromator was used to tune the incident x-ray beam to the desired energies. X-ray absorption spectra were collected over the photoemission ranges of core Gd L_{III} (7242.8 eV) and Yb L_{III} (8943.6 eV) edges in fluorescence, at liquid He temperature and room temperature separately. The data were fitted over the reciprocal space range (k range) 3 to 11 $Å^{-1}$ and the real space range (R range) 1 to 4 Å. Sixpack[12] and Feff[13] were used for data analysis.

The EXAFS analysis was complemented with conventional x-ray powder diffraction and an electron microprobe chemical analysis; the former for phase identification and preliminary structural assessment and the latter in order to

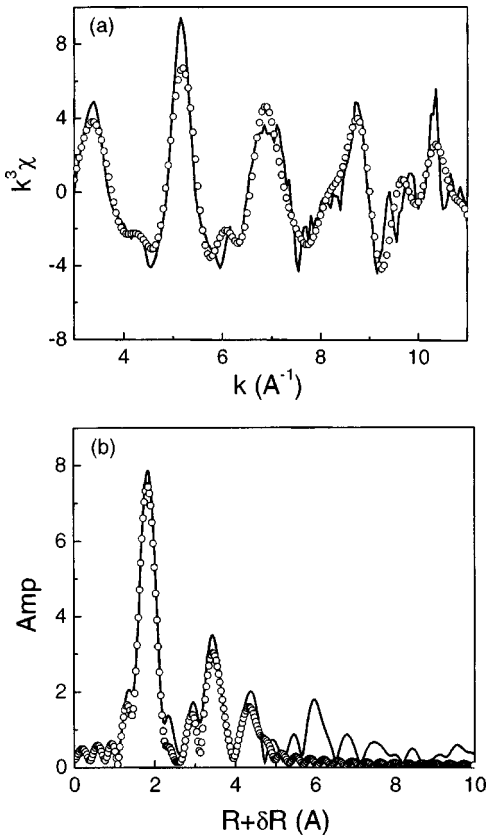

FIG. 4. Yb L_{III} edge EXAFS for $BaCe_{0.85}Gd_{0.15}O_{3-\delta}$ measured at 10 K: experimental data (solid line), best fit data (open circles); (a) the normalized EXAFS spectrum (k^3 weighted), and (b) the Fourier transform without the phase shift.

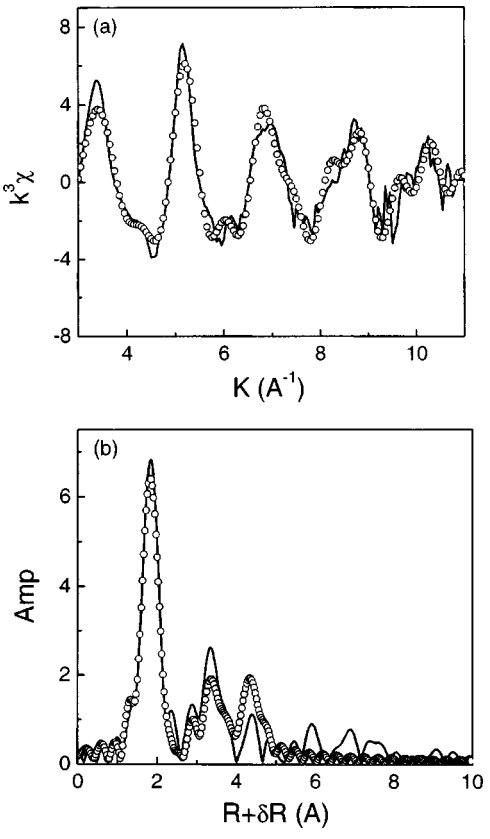

FIG. 5. Yb L_{III} edge EXAFS for $BaCe_{0.85}Gd_{0.15}O_{3-\delta}$ measured at 300 K: experimental data (solid line), best fit data (open circles); (a) the normalized EXAFS spectrum (k^3 weighted), and (b) the Fourier transform without the phase shift.

ascertain the actual, and not merely nominal, stoichiometry of the samples. The methodology and results of both of these sets of experiments have been presented elsewhere for a broad range of compositions including those examined here,[6] and are included, in brief, in the present work to permit a facile comparison to the EXAFS results.

III. SYNTHESIS AND PRELIMINARY CHARACTERIZATION

$BaCe_{0.85}M_{0.15}O_{3-\delta}$ (M=Nd, Gd Yb) powders were synthesized by a chemical solution route as described elsewhere.[6] Briefly, the precursors were $Ba(NO_3)_2$, $Ce(NO_3)_3\cdot 6H_2O$, $Nd(NO_3)_3\cdot 6H_2O$, $Yb(NO_3)_3\cdot 4.44H_2O$ and $Gd(NO_3)_3\cdot 5.45H_2O$ (the water content in the Yb and Gd nitrates was determined by a thermogravimetric analysis). These nitrates were dissolved in a mixture of water and ethylene glycol, with ethylenediaminetetraacetic acid (EDTA) added as a chelating agent. Polymerization of the ethylene glycol occurred upon mild heating, and the resulting char was calcined at 1300 °C for 10 hr and cooled in air at a rate of 20 °C/min, yielding a single perovskite phase. Green pellets (9 mm in diameter) were obtained by dry pressing at 150 MPa and isostatic pressing at 270 MPa. High density pellets ($\geqslant$94% of theoretical) were obtained by sintering in air at 1550 °C for 4 h and cooled in air at a rate of 5 °C/min.

Powder x-ray diffraction measurements showed that the cell volume was not a monotonic function of dopant ionic radius, Fig. 1 and Table III,[14] as has been noted earlier.[6] Diffraction data were collected from calcined powders (Siemens D-500, Cu$K\alpha$ radiation) using nickel powder (99.99%) as an internal standard for the peak position determination. Samples were examined in the as-synthesized, hydrated and dried states, where hydration was achieved by exposing powders to water-saturated argon at 500 °C for 20 hr, and drying by annealing samples at 700 °C under dry air for 6 h. Both hydrated and dried samples were examined by x-ray diffraction immediately following the treatment. Lattice parameters were refined using the program RIETICA[15] and assuming the initial $BaCeO_3$ structure of Knight *et al.*[11] Hydration of the samples leads to an overall increase in cell volume, Fig. 1, but the dependence of volume on dopant species is unchanged. Moreover, the as-synthesized samples, exposed to lab atmosphere for 7 days prior to data collection, have cell volumes comparable to samples intentionally dried. Thus, crystallographic results obtained from an EXAFS analysis of as-synthesized materials refer to the dehydrated state.

An electron microprobe chemical analysis was performed on sintered pellets. Samples were mounted in an epoxy resin, cut, polished and coated with a conductive layer of carbon. Characteristic x-ray emission intensities of the specific elements, measured with JEOL JXA-733 EMP, were converted to chemical weight percents and molar ratios with the program CITZAF[16] and using appropriate standards. Measured chemical compositions are provided along with the

TABLE IV. Model refinement statistics and best-fit structural parameters for the Gd L_{III} edge EXAFS in $BaCe_{0.85}Gd_{0.15}O_{3-\delta}$.

Shell (Gd on B^{4+}-site)	Atom type	Multiplicity	Temp. (10 K) R(Å)	Temp. (10 K) σ^2(Å^2)	Temp. (300 K) R(Å)	Temp. (300 K) σ^2(Å^2)
1	O	2	2.298(7)	0.003(1)	2.298(8)	0.004(1)
2	O	2	2.298(7)	0.003(1)	2.298(8)	0.004(1)
3	O	2	2.298(7)	0.003(1)	2.298(8)	0.004(1)
Ave. Gd–O dist.			2.298		2.298	
4	Ba	2	3.834(10)	0.006(1)	3.860(11)	0.006(1)
5	Ba	2	3.834(10)	0.006(1)	3.860(11)	0.006(1)
6	Ba	2	3.992(3)	0.006(1)	4.004(7)	0.006(1)
7	Ba	2	3.992(3)	0.006(1)	4.004(7)	0.006(1)
Ave.Gd–Ba dist.			3.913		3.932	
Shell (Gd on A^{2+}-site)	Atom type	Multiplicity	R(Å)	σ^2(Å^2)	R(Å)	σ^2(Å^2)
8	O	1	2.463(11)	0.001(1)	2.465(11)	0.001(1)
9	O	2	2.463(11)	0.001(1)	2.465(11)	0.001(1)
10	O	2	2.467(2)	0.001(1)	2.467(10)	0.001(1)
11	O	1	2.467(2)	0.001(1)	2.467(10)	0.001(1)
12	O	2	2.467(2)	0.001(1)	2.467(10)	0.001(1)
13	O	1	2.467(2)	0.001(1)	2.467(10)	0.001(1)
14	O	2	2.470(3)	0.001(1)	2.470(4)	0.001(1)
15	O	1	2.470(3)	0.001(1)	2.470(4)	0.001(1)
Ave. Gd–O dist.			2.467		2.467	
16	Ce	2	3.752(12)	0.001(1)	3.757(14)	0.002(1)
17	Ce	2	3.752(12)	0.001(1)	3.757(14)	0.002(1)
18	Ce	2	3.752(12)	0.001(1)	3.757(14)	0.002(1)
19	Ce	2	3.752(12)	0.001(1)	3.757(14)	0.002(1)
Ave.Gd–Ce dist.			3.752		3.757	
Frac			0.869(10)		0.866(9)	
k range			(3,11)		(3,11)	
Chi^2			1.71		2.89	
R factor			0.0223		0.022	

EXAFS results (see below). It should be noted that because increased BaO loss and dopant incorporation onto the barium site are expected with high temperature processing,[4–6] the microprobe results, obtained from sintered pellets, are not directly comparable to the EXAFS and diffraction results, obtained from calcined powders. Rather, a similarity in general trends with a dopant species is expected.

IV. EXAFS RESULTS AND DISCUSSION

The oscillatory EXAFS spectra of Gd L_{III} and Yb L_{III} edges with the corresponding Fourier transforms are shown in Figs. 2–5. The first two present the 10 and 300 K spectra, respectively, for Gd and the latter two the spectra for Yb. In all cases, the experimental data are compared with the best fit. The structural parameters and refinement statistics obtained from the fitting procedure are summarized in Tables IV and V for Gd and Yb, respectively. The refinement proceeded smoothly, yielding final residuals in the range 0.022 −0.041, and χ^2 values in the range 1.7–25. The defect chemical parameters and overall stoichiometries implied by the fitted models are summarized in Table VI, where they are also compared with the results of the x-ray powder diffraction analysis and electron microprobe chemical analysis.

The results of Tables IV–VI reveal several important points. Most significant is that measurable dopant site partitioning indeed occurs, with the *frac* parameter differing from a value of 1 by several standard deviations for both compositions. Furthermore, as anticipated and consistent with previous studies,[6] the extent of Yb incorporation onto the A site (~4%) is less than Gd incorporation onto that site (~13%). From an analysis of the cell volumes, Fig. 1, the extent of Yb, Gd and Nd incorporation onto the Ba site was inferred to be 4.6, 7.2, and 14%,[6] respectively, the first two values being in reasonable agreement with the present EXAFS results. Similarly qualitative, though not quantitative, agreement is found with the results of the electron microprobe chemical analysis. The chemical analysis measurements showed Ba:(Ce+M) molar ratios of 0.996, 0.976 and 0.913 for Yb, Gd and Nd, respectively, whereas the ratios implied by the EXAFS results for the first two dopant species are 0.989 and 0.961, respectively (at 10 K). Although the Nd EXAFS experiments could not be performed, one can extrapolate from the results obtained for Yb and Gd and conclude that Nd incorporation onto the Ba site would be greater than the 13% measured here for Gd, and the Ba:(Ce+M) ratio lower than 0.961. As a consequence of the dopant partitioning, the con-

TABLE V. Model refinement statistics and best-fit structural parameters for the Yb L_{III} edge EXAFS in $BaCe_{0.85}Yb_{0.15}O_{3-\delta}$.

Shell (Yb on B^{4+}-site)	Atom type	Multi-plicity	Temp. (10 K) R(Å)	Temp. (10 K) σ^2(Å^2)	Temp. (300 K) R(Å)	Temp. (300 K) σ^2(Å^2)
1	O	2	2.239(4)	0.005(1)	2.242(5)	0.007(1)
2	O	2	2.239(4)	0.005(1)	2.242(5)	0.007(1)
3	O	2	2.239(4)	0.005(1)	2.242(5)	0.007(1)
Ave. Yb–O dist.			2.239		2.242	
4	Ba	2	3.708(5)	0.006(1)	3.734(4)	0.008(2)
5	Ba	2	3.708(5)	0.006(1)	3.734(4)	0.008(2)
6	Ba	2	3.853(6)	0.006(1)	3.890(5)	0.008(2)
7	Ba	2	3.853(6)	0.006(1)	3.890(5)	0.008(2)
Ave. Yb–Ba dist.			3.781		3.812	
Shell (Yb on A^{2+}-site)	Atom type	Multiplicity	R(Å)	σ^2(Å^2)	R(Å)	σ^2(Å^2)
8	O	1	2.414(8)	0.002(1)	2.416(8)	0.003(1)
9	O	2	2.414(8)	0.002(1)	2.416(8)	0.003(1)
10	O	2	2.414(8)	0.002(1)	2.416(8)	0.003(1)
11	O	1	2.414(8)	0.002(1)	2.416(8)	0.003(1)
12	O	2	2.417(8)	0.002(1)	2.420(7)	0.003(1)
13	O	1	2.417(8)	0.002(1)	2.420(7)	0.003(1)
14	O	2	2.417(8)	0.002(1)	2.420(7)	0.003(1)
15	O	1	2.417(8)	0.002(1)	2.420(7)	0.003(1)
Ave. Yb–O dist.			2.416		2.418	
16	Ce	2	3.678(8)	0.002(1)	3.679(8)	0.008(2)
17	Ce	2	3.678(8)	0.002(1)	3.679(8)	0.008(2)
18	Ce	2	3.678(8)	0.002(1)	3.679(8)	0.008(2)
19	Ce	2	3.678(8)	0.002(1)	3.679(8)	0.008(2)
Ave.Yb–Ce dist.			3.678		3.679	
Frac			0.964(8)		0.953(12)	
k range			(3,11)		(3,11)	
Chi^2			25.48		20.26	
R factor			0.0311		0.0413	

centration of oxygen vacancies is reduced, as inferred from the EXAFS analysis, from the desired value of 7.5 mol% of the oxygen sites (=1/2 the dopant concentration) to ~7% for Yb and ~5.5% for Gd.

A second important observation is that, upon doping, the structure of barium cerate undergoes local distortions. That is, the distances from the central dopant atom to the nearest neighbors differ from the comparable distances in undoped barium cerate. This distortion results directly from the size "mismatch" between Ba, Ce and the dopants. Furthermore, because the difference in ionic radii is relatively small between Ce and the dopants, the distortion about the B site is substantially less than that about the A site. The mean Ce–O distance in undoped barium cerate is 2.241(4) Å, whereas Gd–O and Yb–O distances for the dopants on the cerium site are 2.298(4) and 2.239(5) Å, respectively. In contrast, the

TABLE VI. Defect chemical parameters and stoichiometry of nominally $BaCe_{0.85}M_{0.15}O_{3-\delta}$ materials (M=Gb,Yb) as derived from EXAFS and compared with the results of x-ray diffraction analysis and microprobe analysis.

Dopant	Gd		Yb	
	10 K	300 K	10 K	300 K
[M] on A-site	0.020(2)	0.021(1)	0.005(1)	0.007(2)
[M] on B-site	0.133(2)	0.133(1)	0.145(1)	0.144(2)
δ	0.056(2)	0.056(1)	0.070(1)	0.068(2)
Ba:(M+Ce)	0.961(3)	0.960(2)	0.989(2)	0.986(4)
Composition by EXAFS at 300 K	$(Ba_{0.980}Gd_{0.020})(Ce_{0.867}Gd_{0.133})O_{2.944}$		$(Ba_{0.993}Yb_{0.007})(Ce_{0.856}Yb_{0.144})O_{2.932}$	
Ba:(M+Ce) by XRD[a]	0.978(0)		0.986(0)	
Composition by XRD[a]	$(Ba_{0.989}Gd_{0.011})(Ce_{0.859}Gd_{0.141})O_{2.935}$		$(Ba_{0.993}Yb_{0.007})(Ce_{0.856}Yb_{0.144})O_{2.932}$	
Ba:(M+Ce) by microprobe analysis[a]	0.976(12)		0.996(12)	
Composition by microprobe analysis[a]	$(Ba_{0.988}Gd_{0.012})(Ce_{0.860}Gd_{0.140})O_{2.936}$		$(Ba_{0.998}Yb_{0.002})(Ce_{0.852}Yb_{0.148})O_{2.927}$	

[a]Cited from Ref. 6.

comparable mean A–O distances are 3.13(30), 2.467(2) and 2.418(3) Å for Ba, Gd and Yb, respectively. It is noteworthy that the introduction of Yb onto the Ce site, in fact, produces almost no local changes in average bond distances. This, combined with the fact that the extent of Yb incorporation on the Ba site is small, indicates that the observed decrease in cell volume upon Yb doping, Fig. 1, is primarily attributable to oxygen vacancies which presumably have a smaller effective ionic radius than occupied oxygen sites.[17] These kinds of detailed observations demonstrate the strength of the EXAFS method over conventional x-ray powder diffraction for the study of defect chemistry. The powder diffraction pattern reveals the average structure, which changes only slightly upon dopant introduction. In contrast, the EXAFS spectrum is highly sensitive to the local structure through distinct changes in the sharp features of the radial distribution function.

A final result to note from the data of Figs. 2–5 and Tables IV and V is the significantly lower thermal disorder in the samples examined at 10 K than at room temperature. In particular, the spectra in Figs. 2 and 4 are sharper than those of Figs. 3 and 5. The derived Debye–Waller factors, σ^2, being slightly smaller for the 10 K refinements, reflect this difference in disorder. The other parameters, however, are comparable for the two temperatures, suggesting no unusual effects on cooling (Tables IV and V).

V. CONCLUSIONS

The dopant site incorporation preference in perovskites of nominal stoichiometry $BaCe_{0.85}M_{0.15}O_{3-\delta}$ (M=Nd,Gd, Yb) has been investigated in depth. By fitting a weighted average of two separate structures, one with the dopant on the A site and the second with the dopant on the B site, EXAFS data, collected for the dopants Gd and Yb, have been accurately modeled. The analysis shows that 4.6% of the Yb and 13.6% of the Gd intended for incorporation onto the Ce site, in nominally stoichiometric $BaCe_{0.85}M_{0.15}O_{3-\delta}$, resides on the Ba site. As a consequence, the concentration of oxygen vacancies is reduced from the ideal value of 7.5 mol% of the oxygen sites (=1/2 the dopant concentration) to ~7% for Yb and ~5.6% for Gd. Accordingly, dopants of larger ionic radii, which exhibit a greater extent of dopant incorporation onto the A^{2+} site, exhibit a lower proton uptake and conductivity upon exposure to humid atmospheres than dopants with smaller ionic radii. In addition, although Yb resides primarily on the Ce site and no measurable local structural distortions in $BaCeO_3$ were observed upon the introduction of this dopant, the overall cell volume of the perovskite decreased noticeably. This is attributed to the smaller effective ionic radii of oxygen vacancies than physically present oxygen ions.

ACKNOWLEDGMENTS

The authors thank Wilhelmia (Lala) Espinosa for help preparing samples, Dr. Chi Ma for assistance with the microprobe chemical analysis and Dr. John Bargar for advice on EXAFS analysis. This work is funded by the Department of Energy, Office of Energy Efficiency and Renewable Energy. Additional support is provided by the National Science Foundation through its support of the Caltech Center for the Science and Engineering of Materials. Portions of this research were carried out at the Stanford Synchrotron Radiation Laboratory, a national user facility operated by Stanford University on behalf of the U.S. Department of Energy, Office of Basic Energy Sciences. The SSRL Structural Molecular Biology Program is supported by the Department of Energy, Office of Biological and Environmental Research, and by the National Institutes of Health, National Center for Research Resources, Biomedical Technology Program.

[1] H. Iwahara, H. Uchida, K. Ono, and K. Ogaki, J. Electrochem. Soc. **135**, 529 (1988).
[2] H. Iwahara, H. Uchida, and K. Morimoto, J. Electrochem. Soc. **137**, 462 (1990).
[3] H. Iwahara, H. Uchida, K. Ogaki, and H. Nagato, J. Electrochem. Soc. **138**, 295 (1991).
[4] D. Shima and S. M. Haile, Solid State Ionics **97**, 443 (1997).
[5] S. M. Haile, G. Staneff, and K. H. Ryu, J. Mater. Sci. **36**, 1149 (2001).
[6] J. Wu, L. P. Li, L. Espinosa, and S. M. Haile, J. Mater. Res. **19**, 2366 (2004).
[7] G. Ma, T. Shimura, and H. Iwahara., Solid State Ionics **120**, 51 (1999)
[8] D. A. Stevenson, N. Jiang, R. M. Buchanan, and F. E. G. Henn, Solid State Ionics **62**, 279 (1993).
[9] B. K. Teo, *EXAFS: Basic Principles and Data Analysis* (Springer-Verlag, Berlin, 1986), pp. 21–31.
[10] R. A. Davies, M. S. Islam, A. V. Chadwick, and G. E. Rush, Solid State Ionics **130**, 15 (2000).
[11] K. S. Knight and N. Bonanos, J. Mater. Chem. **4**, 899 (1994).
[12] S. M. Webb, http://www-ssrl.slac.stanford.edu/~swebb/sixpack.htm.
[13] J. J. Rehr, S. I. Zabinsky, and R. C. Albers, Phys. Rev. Lett. **69**, 3397 (1992).
[14] R. D. Shannon, Acta Crystallogr., Sect. A: Cryst. Phys., Diffr., Theor. Gen. Crystallogr. **A32**, 751 (1976).
[15] IUCR Powder Diffr. **22**, 21 (1997).
[16] J. T. Armstrong, Microbeam Anal. **4**, 177 (1995).
[17] M. Mogensen, D. Lybye, N. Bonanos, P. V. Hendriksen, and F. W. Poulsen, *Electrochemical Society Proceedings* 2002, Vol. 2001-28, p. 15.